Supporting information

In-situ Construction of Medium-Entropy Interface on Manganese-based Prussian Blue Analogues for Aqueous Zinc-ion Batteries

Zining Li,[a,1] Jianhui Cen,[a,1] Yang Li,[a,b] Liubing Dong [a,*]

[a] College of Chemistry and Materials Science, Jinan University, Guangzhou 511443, China

[b] School of Materials and Energy, Foshan University, Foshan 528000, China

* Corresponding author: donglb@jnu.edu.cn

[1] These two authors contributed equally to this work.

2. Supporting images and tables

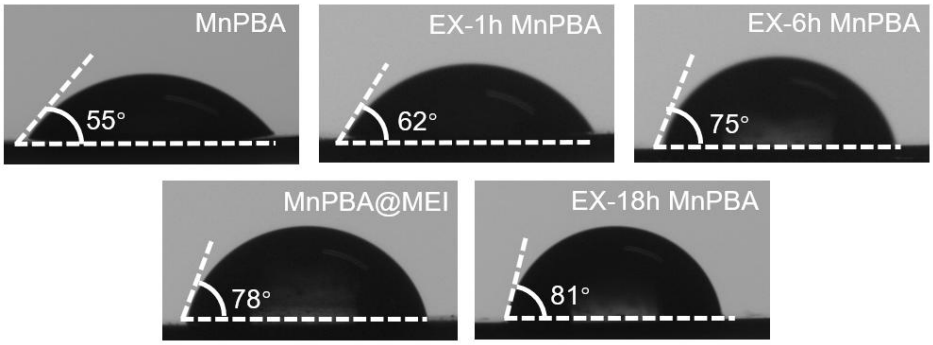

Figure S1. Water contact angles of MnPBA and EX-MnPBA.

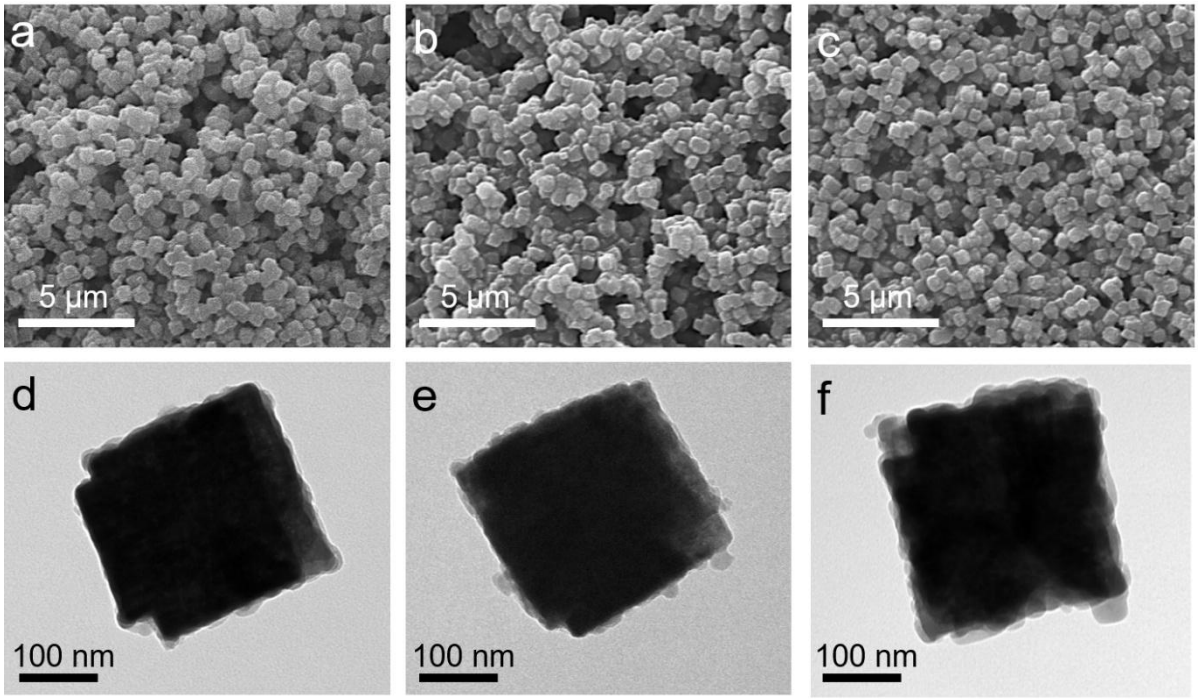

Figure S2. SEM images of (a) EX-1h MnPBA, (b) EX-6h MnPBA, and (c) EX-18h MnPBA samples; TEM images of (d) EX-1h MnPBA, (e) EX-6h MnPBA, and (f) EX-18h MnPBA samples.

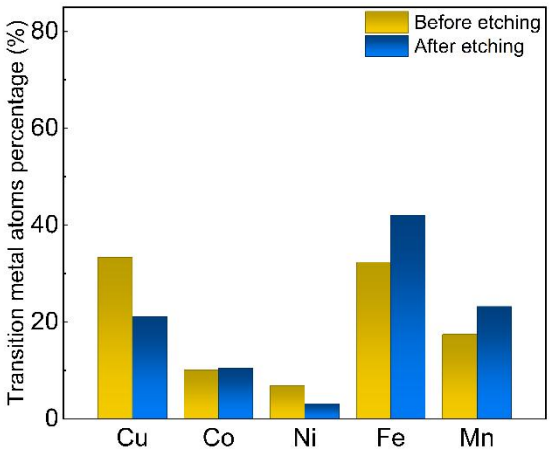

Figure S3. Percentage of transition metal atoms measured by XPS in MnPBA@MEI before and after 40 nm of Ar ion etching.

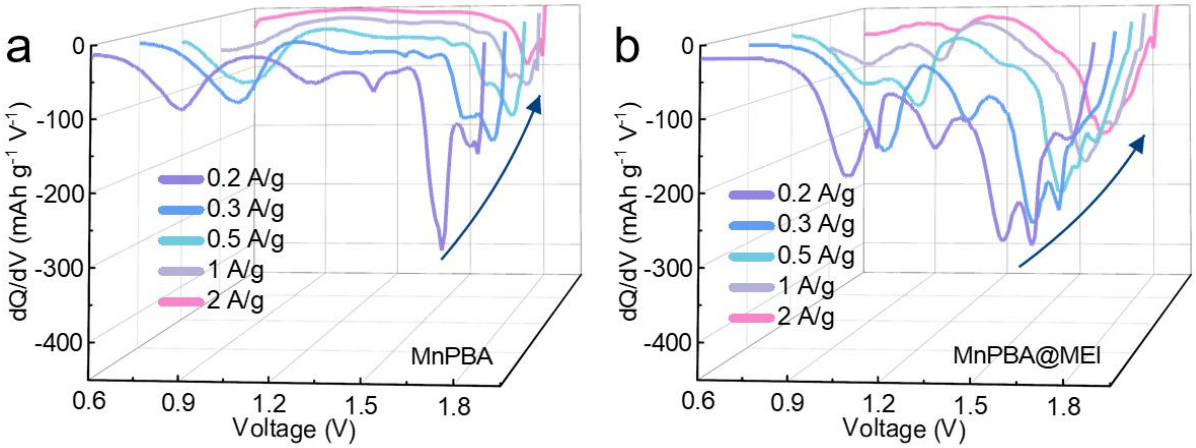

Figure S4. dQ/dV curves of MnPBA and MnPBA@MEI at different current densities.

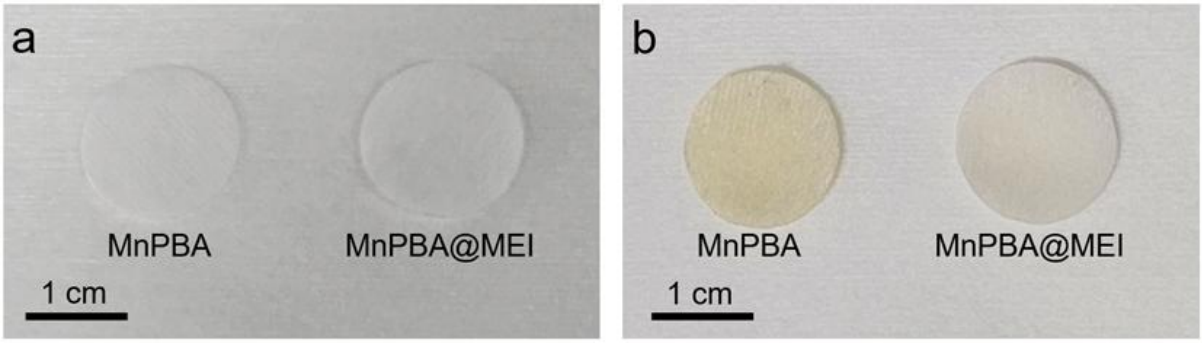

Figure S5. Optical photographs of the separators from batteries assembled with MnPBA and MnPBA@MEI cathodes (a) before cycling and (b) after 100 cycles.

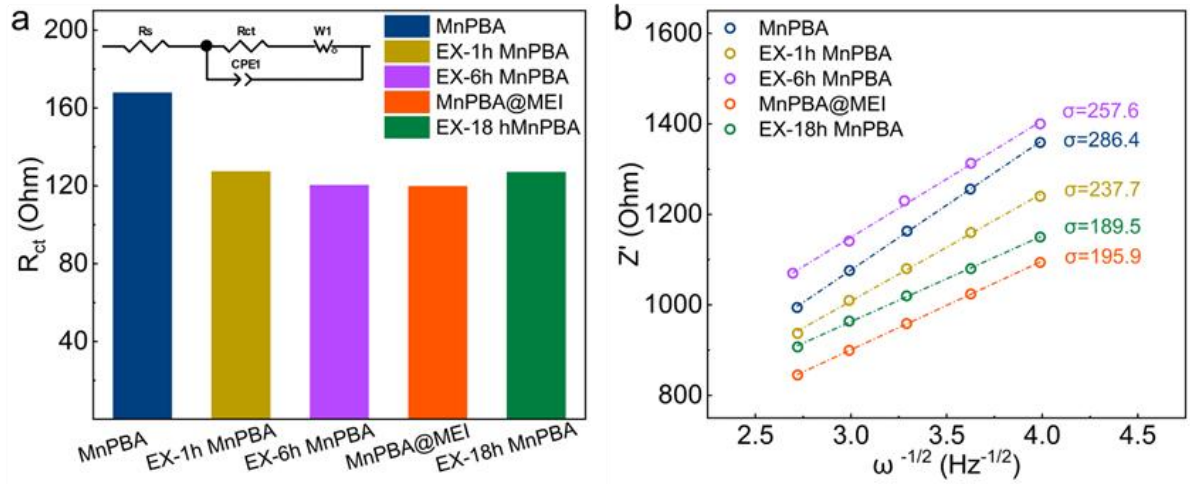

Figure S6. (a) Chargre transfer resistance (with equivalent circuit model embedded) and (b) the fitted lines of Warburg coefficient of the MnPBA and EX-MnPBA cathods. The charge transfer impedance results obtained from EIS fitting show that the electrochemical performance of the MnPBA cathode is significantly improved after ion exchange: Compared to the relatively high R_{ct} of the pristine MnPBA (approximately 168 Ω), the R_{ct} of the ion-exchanged samples decrease significantly (127, 122, 121, and 127 Ω, respectively, as the exchange time increases), indicating a reduction in interfacial charge transfer impedance. Furthermore, the Warburg coefficients obtained from EIS fitting show an overall decreasing trend with increasing ion-exchange time. Among them, the MnPBA@MEI sample exhibits a low σ value, indicating that the medium entropy strategy can optimize interfacial reactions and ion transport, thereby effectively enhancing the electrochemical reaction kinetics of the MnPBA cathode.

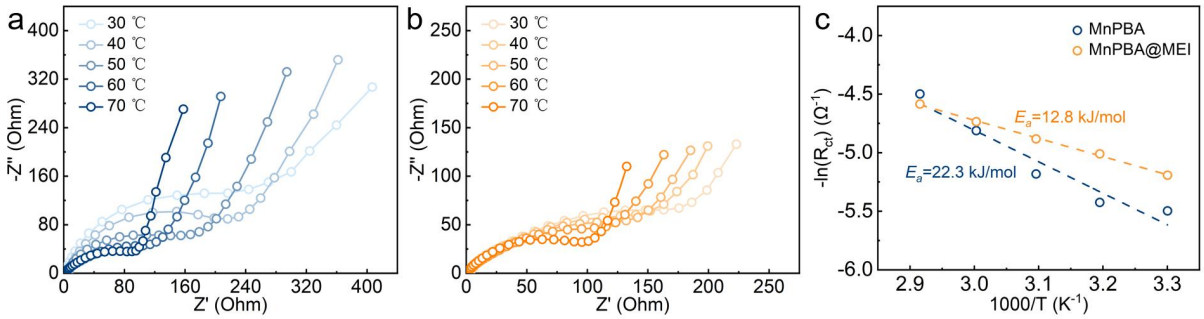

Figure S7. EIS spectra of (a) MnPBA and (b) MnPBA@MEI cathodes at different temperatures; (c) Calculated desolvation activation energies.

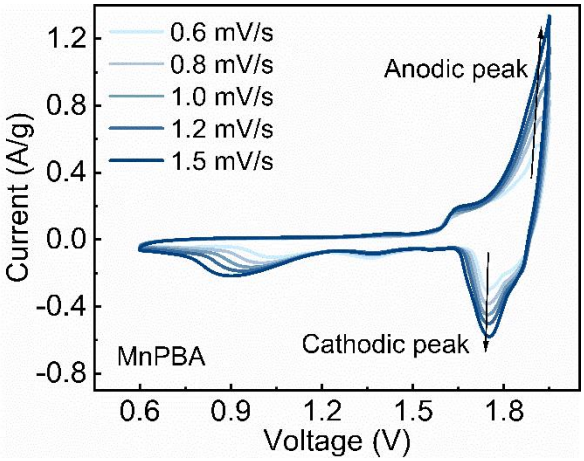

Figure S8. CV curves of MnPBA at different scan rates.

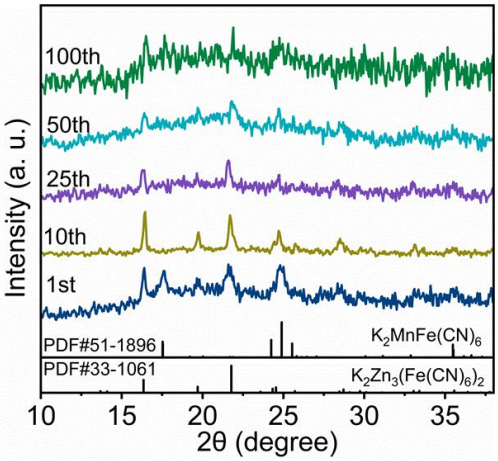

Figure S9. XRD patterns of MnPBA after different numbers of cycles. The pristine MnPBA cathode undergoes severe and rapid structural degradation during the cycling process. Noticeably, as early as the 1st cycle, new diffraction peaks assigned to $K_2Zn_3(Fe(CN)_6)_2$ (PDF#33-1061) emerge clearly. With continuous charge and discharge, the characteristic peaks of the original MnPBA diminish rapidly. By the 25th cycle, the initial crystal framework is almost entirely transformed into the ZnPBA phase. The subsequent 50th and 100th cycles exhibit a drastic decrease in peak intensity and significant broadening, indicating an ongoing irreversible phase transformation accompanied by severe amorphization. This devastating structural collapse, driven by severe Mn dissolution and irreversible Zn^{2+} insertion, sharply highlights the crucial role of the in-situ constructed mid-entropy interface in effectively suppressing harmful phase transitions and guaranteeing the long-term structural integrity of the cathode.

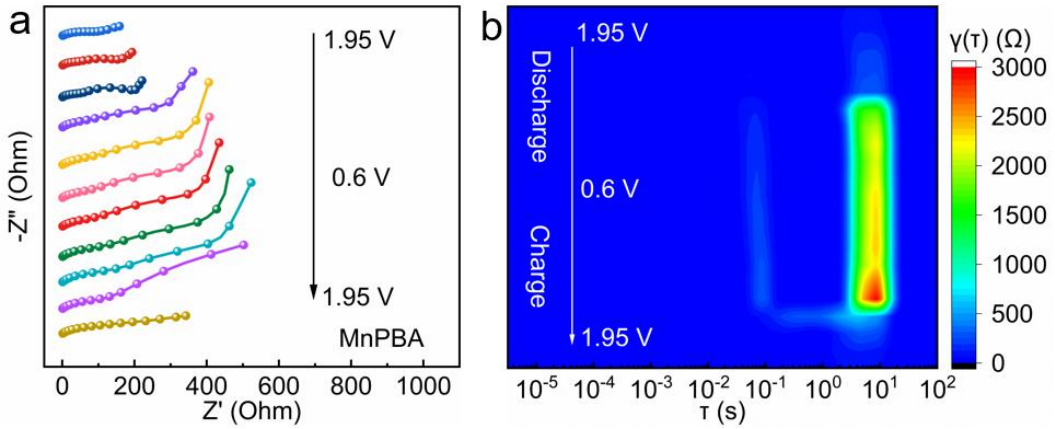

Figure S10. (a) In-situ EIS spectra and (b) corresponding DRT plots of the MnPBA cathode. During the discharge process, both the charge transfer resistance and ion diffusion-related impedance of the MnPBA cathode exhibit a continuous and significant increase, which fails to recover during the subsequent charging process. This irreversible impedance growth stems from the severe interfacial degradation and structural instability experienced by the pristine MnPBA cathode during cycling, ultimately leading to rapid capacity decay and poor cycling performance.

Table S1. Atomic percentage of elements in MnPBA@MEI sample based on XPS analysis.

Sample	Fe (%)	Mn (%)	Co (%)	Ni (%)	Cu (%)
MnPBA@MEI	3.34	1.80	1.04	0.71	3.44

Table S2. Inductively coupled plasma-optical emission spectroscopy for MnPBA and EX-MnPBA.

	Mn (wt%)	Fe (wt%)	Co (wt%)	Ni (wt%)	Cu (wt%)
MnPBA	13.62	13.92	/	/	/
EX-1h MnPBA	9.93	13.43	0.25	0.26	11.41
EX-6h MnPBA	8.55	13.64	0.44	0.49	10.56
MnPBA@MEI	7.43	12.71	0.65	0.70	11.86
EX-18h MnPBA	6.96	12.90	0.56	0.60	15.41

Note: Data are presented as mean of three independent measurements.

Table S3. Comparison of the zinc-ion storage performance of the MnPBA@MEI cathode with literature-reported Prussian blue analogues.

Cathode	Electrolyte	Capacity (mAh/g)	Rate capability (mAh/g)	*Ref.*
MnPBA@MEI	2 M $ZnSO_4$	133 (0.2 A/g)	76 (2 A/g)	This work
CuMn-PBA	3 M LiTFSI + 2 M $Zn(CF_3SO_3)_2$	117 (0.1 A/g)	66 (2 A/g)	[S1]
CoNiHCF/CNTs-20	3 M $ZnSO_4$	95 (0.1 A/g)	44 (1 A/g)	[S2]
VHCF/CNTs	2 M $ZnSO_4$	100 (0.05 A/g)	24 (1.6 A/g)	[S3]
KMHCF-PVP-80	1 M $ZnSO_4$ + 0.1M $MnSO_4$	95 (0.1 A/g)	40 (0.4 A/g)	[S4]
HE-PBA	3 M $Zn(CF_3SO_3)_2$	89 (0.1 A/g)	45 (2 A/g)	[S5]
NiHCF/RGO	2 M $ZnSO_4$	95 (0.005 A/g)	50 (0.2 A/g)	[S6]
CoMnHCF	1 M $ZnSO_4$ + 0.5 M Na_2SO_4	120 (0.1 A/g)	35 (1 A/g)	[S7]
CoHCF	2 M $ZnSO_4$	105 (0.2 A/g)	66 (1 A/g)	[S8]
PDA@MnPBA	4 M $Zn(OTF)_2$	87 (0.05 A/g)	54 (2 A/g)	[S9]

References

[S1] Y. Zeng, J. Xu, Y. Wang, S. Li, D. Luan and X. Lou. Formation of CuMn Prussian blue analog double-shelled nanoboxes toward long-life Zn-ion batteries, *Angew. Chem. Int. Edit.*, 2022, **61**, e202212031.

[S2] J. Cao, Y. Xue, Z. Ji, J. Pu, X. Shen, L. Kong and A. Yuan, CoNi hexacyanoferrate nanoparticles anchored on carbon nanotubes as superior cathode materials for rechargeable

aqueous zinc-ion batteries, *J. Energy Storage,* 2024, **86**, 111413.

[S3] Y. Xue, X. Shen, H. Zhou, J. Cao, J. Pu, Z. Ji, L. Kong and A. Yuan, Vanadium hexacyanoferrate nanoparticles connected by cross-linked carbon nanotubes conductive networks for aqueous zinc-ion batteries, *Chem. Eng. J.*, 2022, **448**, 137657.

[S4] T. Cao, F. Zhang, M. Chen, T. Shao, Z. Li, Q. Xu, D. Cheng, H. Liu and Y. Xia, Cubic manganese potassium hexacyanoferrate regulated by controlling of the water and defects as a high-capacity and stable cathode material for rechargeable aqueous zinc-ion batteries, *ACS Appl. Mater. Interfaces*, 2021, **13**, 26924.

[S5] J. Xing, Y. Zhang, Y. Jin and Q. Jin, Active cation-integration high-entropy prussian blue analogues cathodes for efficient Zn storage, *Nano Res.*, 2023, **16**, 2486.

[S6] Y. Xue, Yao Chen, X. Shen, A. Zhong, Z. Ji, J. Cheng, L. Kong and A. Yuan, Decoration of nickel hexacyanoferrate nanocubes onto reduced graphene oxide sheets as high-performance cathode material for rechargeable aqueous zinc-ion batteries, *J. Colloid Interface Sci.*, 2022, **609**, 297.

[S7] D. Wang, Z. Zhou, T. Ma, J. Zhang, Y. Zhang, R. Ma, D. Zhang and T. Yan, In situ electrochemical Mn vacancies in CoMnHCF for a high level of zinc storage, *Chem. Commun.,* 2024, **60**, 4080.

[S8] Y. Tang, G. Ma, J. Li, M. Liu, B. Xiao and P. Wang, Cobalt Hexacyanoferrate cathode with stable structure and fast kinetics for aqueous zinc-ion batteries. *ACS Appl. Mater. Interfaces* 2025, **17**, 6560.

[S9] H. Ouyang, H. Zhang, K. Wang, L. Luo, H. Li, J. Liu and S. Chen, A polydopamine-coated strategy of Mn-based prussian blue cathode enabled Mn dissolution suppression for aqueous zinc ion batteries, *Batteries Supercaps,* 2025, **8**, e2500247.